coatings

MDPI

Article

Active Broadband Absorber Based on Phase-Change Materials Optimized via Evolutionary Algorithm

Jing Ma [1], Yonghong Tian [1,*], Jingyi Cheng [2], Shubo Cheng [1], Bin Tang [3], Jing Chen [4], Yougen Yi [5], Pinghui Wu [6], Zao Yi [7] and Tangyou Sun [8,*]

[1] School of Physics and Optoelectronic Engineering, Yangtze University, Jingzhou 434023, China; majing0415@163.com (J.M.); shubocheng@yangtzeu.edu.cn (S.C.)
[2] School of Computing, Queen's University, Kingston, ON K7L 2N8, Canada; 17jc66@queensu.ca
[3] School of Microelectronics and Control Engineering, Changzhou University, Changzhou 213164, China; btang@cczu.edu.cn
[4] College of Electronic and Optical Engineering, Nanjing University of Posts and Telecommunications, Nanjing 210023, China; jchen@njupt.edu.cn
[5] College of Physics and Electronics, Central South University, Changsha 410083, China; yougenyi@csu.edu.cn
[6] Research Center for Photonic Technology, Fujian Key Laboratory for Advanced Micronano Photonics Technology and Devices & Key Laboratory of Information Functional Material for Fujian Higher Education, Quanzhou Normal University, Quanzhou 362000, China; phwu@zju.edu.cn
[7] Joint Laboratory for Extreme Conditions Matter Properties, Tianfu Institute of Research and Innovation, State Key Laboratory of Environmental Friendly Energy Materials, Key Laboratory of Manufacturing Process Testing Technology of Ministry of Education, Southwest University of Science and Technology, Mianyang 621010, China; yizaomy@swust.edu.cn
[8] Guangxi Key Laboratory of Precision Navigation Technology and Application, Guilin University of Electronic Technology, Guilin 541004, China
* Correspondence: yhtian@yangtzeu.edu.cn (Y.T.); suntangyou@guet.edu.cn (T.S.)

Abstract: This article proposes a temperature-controlled absorber based on VO_2, which consists of five layers: a disk-shaped VO_2 layer array, a dielectric layer, a circular hole VO_2 array, a SiO_2 layer, and a gold substrate from top to bottom. We optimized the thickness of the other four layers of the absorber, except for the gold layer, using PSO. After ten iterations, we determined that the optimal parameters for the top-to-bottom four-layer thicknesses were 0.183 μm, 0.452 μm, 0.557 μm and 1.994 μm. At this point, our absorber reached the optimal absorption parameters, and we plotted the absorption spectrum under these conditions. We found that the absorption rate at 29.1–47.2 THz was higher than 90%, and the absorption bandwidth was as high as 18.1 THZ. This frequency band covers most of the atmospheric window area (23–37.5 THz), so it will have good practicality. At 30.8 THz and 43.12 THz, there were perfect absorption peaks with absorption rates of 99.99% and 99.99%, respectively. We explained the cause of absorption from the perspective of electric field, and then we studied the change in the absorption curve of the absorber when the temperature of VO_2 changed, and we can directly observe the changes in the electric field to explain this. Finally, we can tune the bandwidth and absorption rate of the absorber by changing the structure of the VO_2 pattern. After comparing with other absorbers developed in recent years, our absorber still has good competitiveness, and we believe that our solution is expected to have outstanding performance in fields such as photothermal conversion and thermal stealth in the future.

Keywords: VO_2; evolutionary algorithm; broadband absorber; mid-infrared

Citation: Ma, J.; Tian, Y.; Cheng, J.; Cheng, S.; Tang, B.; Chen, J.; Yi, Y.; Wu, P.; Yi, Z.; Sun, T. Active Broadband Absorber Based on Phase-Change Materials Optimized via Evolutionary Algorithm. *Coatings* **2023**, *13*, 1604. https://doi.org/10.3390/coatings13091604

Academic Editor: Dimitrios Tasis

Received: 10 August 2023
Revised: 7 September 2023
Accepted: 13 September 2023
Published: 14 September 2023

1. Introduction

A metamaterial is a synthetic material, which means it is not naturally occurring. Because of metamaterial's customizable electromagnetic properties, it can readily exhibit electromagnetic characteristics that natural materials lack, thus greatly expanding the potential applications of metamaterials [1–6]. In the field of absorbers, the research of Landy's team in 2008 led to the upsurge of applying metamaterials to absorbers [7]. Since then, metamaterial absorbers have been widely used in thermal radiation absorption, optical stealth, intelligent windows and other fields [8–12], while metamaterial narrowband absorbers have outstanding performance in sensor, detection and other fields [13–17].

At present, metamaterials such as Dirac metal, Graphene, and VO_2 are most widely used in metamaterial absorbers [18–22]. This is due to the phase-change characteristics of VO_2 discovered by Bell Labs in 1959 [23], namely that VO_2 is in an insulating state at room temperature, and when it is heated to 340 K, it transitions into a metallic state. Because the phase-change temperature is closer to room temperature than other materials, researchers have always been enthusiastic about VO_2 research. In 2021, Zhong [24] proposed an absorber based on a combination of gold and VO_2 layers. The pattern of the absorber is composed of a cross-shaped array, with a broadband absorption rate of over 90% at 17–26 THz. In 2023, Kwang's [25] team proposed an absorber based on a toroidal VO_2 array. The absorber has three broadband absorption peaks with an absorption bandwidth of more than 2.42 THz and an absorption rate of more than 90% in the terahertz band. So far, the proposed broadband absorber based on VO_2 has an absorption rate of more than 90%, and the absorption bandwidth is mostly within 10 THz, rarely more than 10 THz. The development direction of broadband absorber must aim for a broader absorption bandwidth while maintaining high absorption rates, which is the direction that researchers need to focus on.

Particle swarm optimization (PSO) is a randomized algorithm proposed by James and Russell in 1995. Inspired by the foraging behavior of birds, PSO initializes the algorithm to randomly assign each particle in the search space, and at the same time, it gives each particle an adaptive speed. Particles can remember the best position they have ever been to, and particle are influenced by three factors: the best position it has ever been to, the best global position, and the initial velocity, resulting in a composite acceleration that iterates to the optimal solution [26]. Compared with other optimization algorithms, PSO has the advantages of wide application range, high computing efficiency, and adaptive adjustment of search strategies.

In this article, we propose a double-layer VO_2 absorber based on a circular hole and disk array, and we optimize its parameters with an improved PSO. The results show that in the frequency range of 29.1–47.2 THz, the absorption rate is above 90%, and the total absorption bandwidth is as high as 18.1 THz. When VO_2 transitions from an insulating state to a metallic state, the highest absorption rate of the absorber increases from 10.3% to 99.99%. We explained the reason for this transition from the perspective of an electric field. Furthermore, we discussed the impact of changing structural parameters on the absorber and addressed the effect of changing the incident angle on the absorber toward the end of the article. Our absorbers have good application prospects in fields such as solar energy absorption and stealth coatings.

2. Particle Swarm Optimization

Earlier, we mentioned the basic concept of PSO. We know that the most important thing in PSO is to iterate the position and speed of particles as well as the optimization strategy [27,28]. Although the traditional PSO is convenient to search the optimal solution globally, it takes a long time to search locally, so we chose the improved particle swarm optimization algorithm. The iteration formula of speed and position is as follows [29,30]:

$$newv = wv + c_1 * rand * (gbest - x) + c_2 * rand * (pbest - x) \tag{1}$$

$$newx = x + newv \tag{2}$$

$$w = w_{max} - \frac{d}{maxd} * w_{min} \tag{3}$$

where w is the inertia weight, v and x are the current velocity and position, $newv$ and $newx$ are the updated velocity and position, c_1 and c_2 are acceleration constants, $rand$ is a random number within 1, and $gbest$ and $pbest$ are global and local optimal parameters, respectively. We have defined the weight w that varies with the number of iterations, as shown in Formula (3). We define w_{max} as 0.9 and w_{min} as 0.4. This way, as the iteration progresses, the algorithm switches from searching for global optimal values to searching for local optimal values, greatly enhancing the accuracy and efficiency of the search [31].

In the combination of absorbers and the PSOs in the past, most researchers often choose the average absorption rate of the region as the figure of merit (FOM), which ignores the need for broadband absorbers to meet a wider absorption bandwidth. Therefore, after discussion, we define the formula of FOM as follows [32–34]:

$$FOM = bw_{pre}/bw_{total} \tag{4}$$

where bw_{pre} is the absorption bandwidth with an absorption rate higher than 90%, and bw_{total} is the total bandwidth selected.

Unfortunately, due to the inherent nature of the algorithm, PSO algorithm cannot be well applied in the current hot field of hypersurface inverse design, like random forest (RF) and deep learning (DP). However, in terms of optimization problems, PSO has rare advantages compared to the above two algorithms.

3. Design and Method

As shown in Figure 1a, the absorber we designed has a five-layer structure, consisting of a disk VO_2 array, a Topas layer, a circular hole VO_2 array, a SiO_2 layer, and a gold layer from top to bottom. Among them, the radius of circular VO_2 is r_1 = 0.5 μm, the thickness t_1 = 0.183μm, the refractive index of dielectric layer is 2.35 [35,36], the thickness t_2 = 0.452 μm, the radius of circular hole VO_2 is r_2 = 0.29 μm, the thickness t_3 = 0.557 μm, the refractive index of SiO_2 layer is 1.90, the thickness t_4 = 1.994 μm, and the dielectric constant of the bottom gold layer is described using the drude model, where the plasma frequency $\omega_p = 1.37 \times 10^{16}\ s^{-1}$, and the damping constant $\gamma = 1.23 \times 10^{14}\ s^{-1}$, with a thickness t_5 = 0.2 μm [37,38]. Due to the difficulty in making the absorber we proposed, we have proposed the following production method: first, we deposit a layer of gold on a silicon wafer as the base, and then we prepare a SiO_2 layer on the gold through chemical vapor deposition. Then, VO_2 thin films are generated through magnetron sputtering, and circular holes are generated through chemical etching. For the top layer of VO_2 disk, due to its small thickness, ion beam etching can be used to generate it.

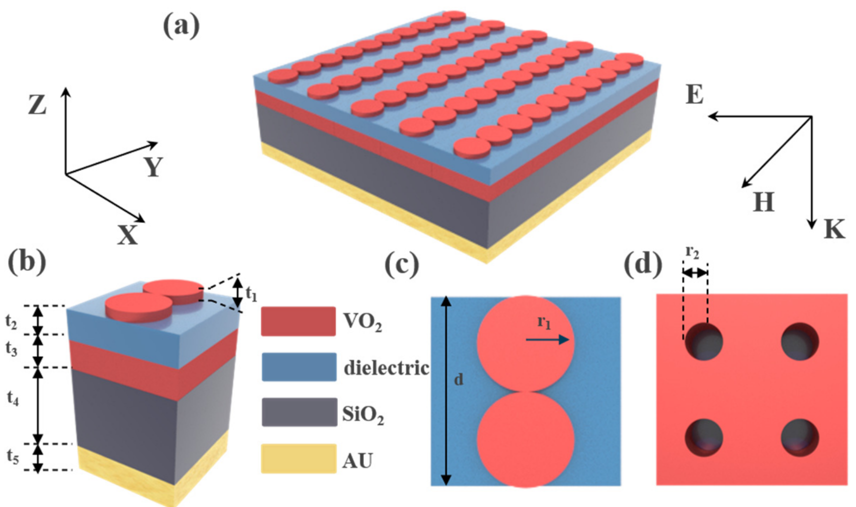

Figure 1. (**a**) 3D diagram of the array absorber structure; (**b**) 3D diagram of unit absorber structure; (**c**) top VO_2 plan view; (**d**) bottom VO_2 plan view.

The dielectric constant of VO_2 can be described by the following drude model [39,40]:

$$\varepsilon(\omega) = \varepsilon_\infty - \frac{{\omega_p}^2}{\omega(\omega + i\gamma)} \tag{5}$$

where $\varepsilon_\infty = 12$, damping frequency $\gamma = 5.75 \times 10^{13}$ rad/s, plasma frequency $\omega_p(\sigma) = \omega_p(\sigma_0)\sqrt{\sigma/\sigma_0}$, where $\omega_p(\sigma_0) = 1.4 \times 10^{15}$ rad/s $\sigma_0 = 3 \times 10^5$ S/m, and without specific instructions, we use the conductivity $\sigma = 2 \times 10^6$ S/m of VO_2 at a temperature of 345 K. We use FDTD Commercial software (Lumerical_2020 R2) for simulation, and the input light wave is the TE wave perpendicular to the absorber surface [41,42]. (See Table 1).

Table 1. Selected parameters and their ranges and minimum accuracy.

Variable	Range (μm)	Minimum Accuracy (μm)
t_1	0.1–0.3	0.001
t_2	0.3–0.6	0.001
t_3	0.5–0.6	0.001
t_4	1.5–2.5	0.001

The iterative operation of FOM is shown in Figure 2b. When the iteration reaches the tenth time, the optimal solution is obtained. Compared with DP, which requires thousands of training sets and genetic algorithms that require at least fifteen iterations [43], PSO has better speed to achieve the optimal value. The optimal values of the four parameters we obtain are t_1 = 0.183 μm, t_2 = 0.452 μm, t_3 = 0.557 μm, and t_4 = 1.994 μm, respectively. At this point, our absorber reaches its maximum bandwidth above 90%:

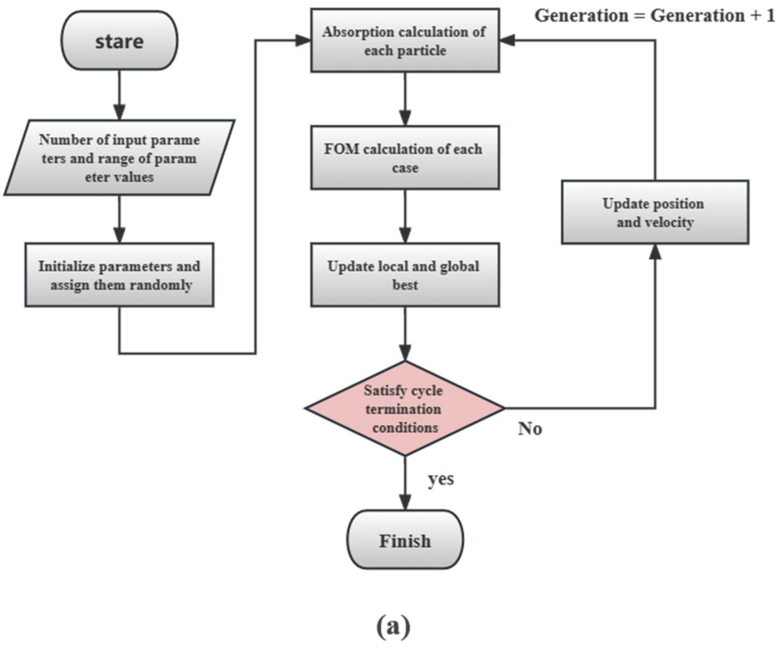

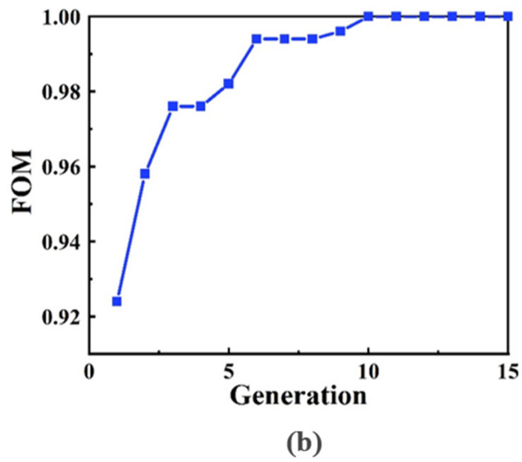

Figure 2. (**a**) PSO algorithm flowchart; (**b**) optimizing the FOM process using PSO.

4. Results and Discussions

Figure 3 shows the absorption spectrum of our absorber. The black curve in the figure shows the absorption curve when both the upper and lower layers of VO_2 are present, the orange curve shows the absorption curve when removing the top VO_2, the blue curve shows the absorption curve when removing the bottom VO_2 layer, the green curve shows the absorption curve when removing the upper dielectric layer, and the red curve shows the absorption curve when removing the SiO_2 layer. At this point, we can clearly see that when we remove any layer structure, the absorption rate can reach up to 97.23%, and the absorption bandwidth above 90% can only reach up to 6.73 terahertz. However, when the five-layer structure is present, the absorption rate can reach up to 99.99%. The absorption bandwidth above 90% is 29.1–47.2 THz, with a maximum of 18.3 THz. The absorption rates at frequencies of 30.74 THz and 43.36 THz reach 99.99% and 99.98%, respectively, achieving perfect absorption. At this time, our absorber has good bandwidth and absorption rate. At the same time, the range of 23–37.5 THz is the atmospheric window, which has a high overlap with our absorption frequency band, which expands the application range of our absorber.

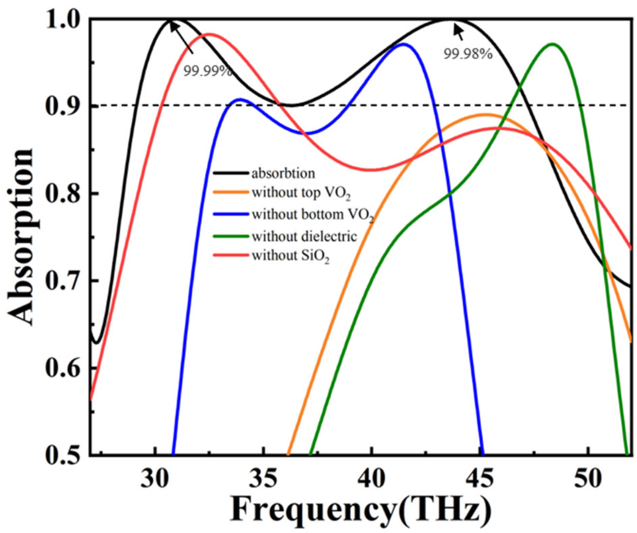

Figure 3. The black curve represents the original absorption curve of the absorber, the orange curve shows the absorption curve when removing the top VO_2 layer, the blue curve shows the absorption curve when removing the bottom VO_2 layer, the green curve shows the absorption curve when removing the upper dielectric layer, and the red curve shows the absorption curve when removing the SiO_2 layer.

In order to explore the reason for the change of absorption rate and absorption bandwidth, we give an explanation from the perspective of electric field.

Figures 4a and 5a show the absorption spectra in the XY direction when both the double layer VO_2 layer and only the top VO_2 layer exist. From these two figures, we can intuitively see that when the bottom VO_2 layer is removed, the intensity of the electric field in the upper layer VO_2 decreases. At the same time, the electric field attached to the x direction of the disk undergoes some dissipation, flowing towards the surrounding medium, resulting in a decrease in absorption [44,45]. Figures 4b–d and 5b–d shows the absorption spectra of the bottom VO_2 layer in the XY, XZ, and YZ directions. Figure 4b–d show the absorption spectra when the top VO_2 layer exists, and Figure 5b–d show the absorption spectra when the top VO_2 layer is removed. From Figure 5b–d, we can see that when there is only the bottom VO_2 layer, the electric field undergoes large-scale resonance in the cavity inside the circular hole and the upper layer of the ring. Local surface plasmon resonance occurs at the bottom of the circular hole, and the intensity of the electric field is also low [46,47]. From Figure 4b–d in comparison, we can see from the electric field graph in the XY direction that the large-scale resonance inside the circular hole has disappeared. By observing the electric field patterns in the XZ and YZ directions, we found that surface plasmon resonance appeared in the upper layer of the circular hole, and the overall electric field intensity also increased significantly, enhancing the absorption of light [48,49]. In summary, the presence of double-layer VO_2 enhances the local surface plasmon resonance of VO_2, reduces large-scale resonance, and increases the absorption of light via the absorber, which explains why we use double-layer VO_2.

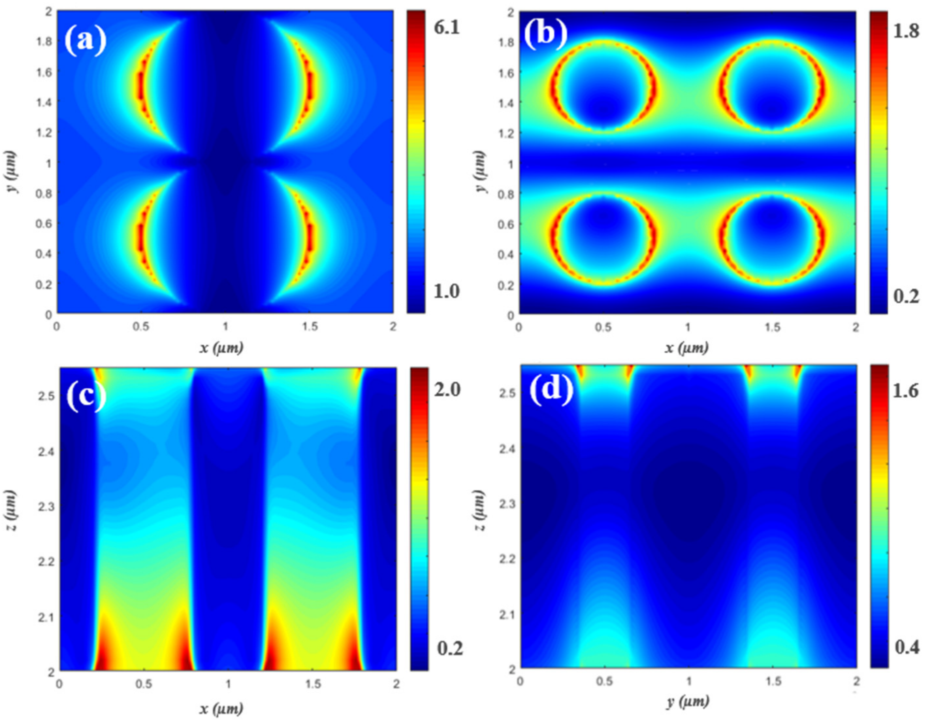

Figure 4. (**a**) The electric field diagram of the upper VO_2 layer of the absorber we proposed in the XY direction; (**b**) the electric field diagram of the lower VO_2 layer of the absorber we proposed in the XY direction; (**c**) the electric field diagram of the lower VO_2 layer of the absorber we proposed in the XZ direction; (**d**) the electric field diagram of the lower VO_2 layer in the YZ direction of our proposed absorber.

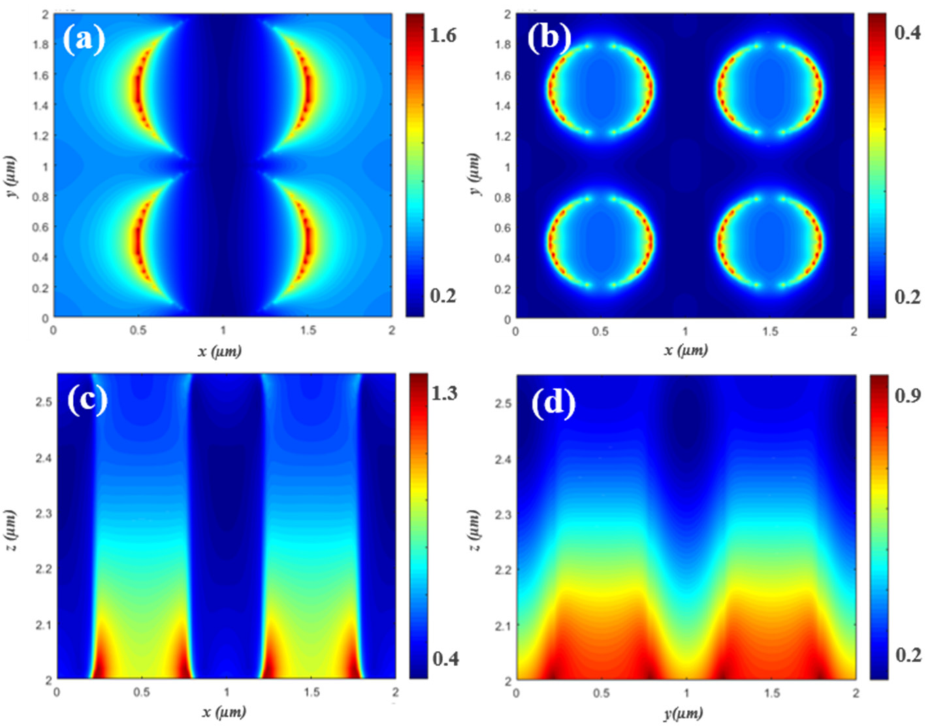

Figure 5. When removing the lower layer VO_2, (**a**) shows the electric field diagram of the upper layer VO_2 in the XY direction of our proposed absorber; when removing the upper layer VO_2, (**b**) shows the electric field diagram of the lower layer VO_2 in the XY direction of our proposed absorber; (**c**) the electric field diagram of the lower VO_2 layer of the absorber we proposed in the XZ direction; (**d**) the electric field diagram of the lower VO_2 layer in the YZ direction of our proposed absorber.

The specific crystal structure of VO_2 results in its phase transition [50,51]. As shown in Figure 6a, we have plotted the effect of VO_2 at different temperatures on the absorption curve of the absorber under heating, At the same time, we can see the phenomenon of conductivity hysteresis during the heating and cooling processes, which is usually considered to be caused by the combined effect of thermal expansion coefficient and internal stress [52,53]. We found that when VO_2 is at 318 K, which is maintained at a low temperature, the overall absorption rate of the absorber is within 12%. However, when the temperature is heated to 340 K, VO_2 begins to phase change, and the overall absorption rate of the absorber increases, with the highest absorption rate reaching 28.7%. As the temperature further increases, we can see that the absorption bandwidth and overall absorption rate of the absorber are also increasing. At 342 K, the absorption bandwidth with an absorption rate of more than 90% reaches 14 THz, and at 345 K, when the maximum absorption at both ends reaches perfect absorption, the absorption rate is higher than 90%, and the absorption band width reaches 16.9 THz. In conclusion, we can adjust the temperature to make the VO_2 phase change, so as to tune the absorption rate and absorption bandwidth of the absorber, which makes our absorber more flexible in practical applications.

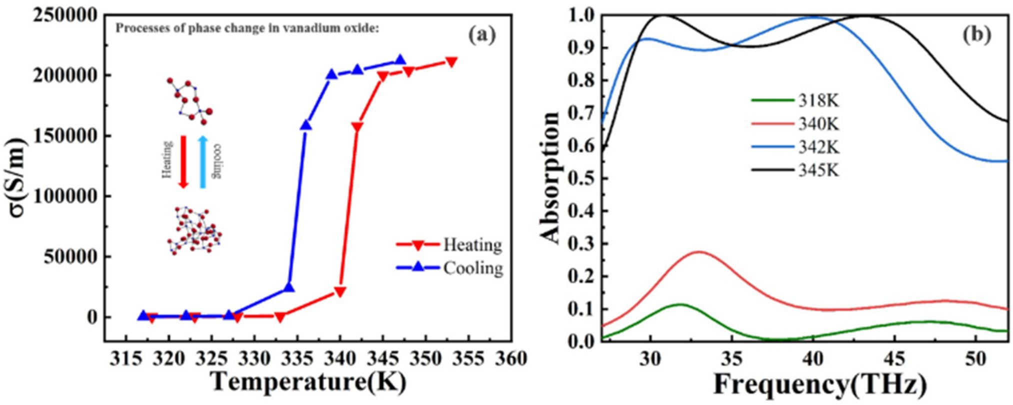

Figure 6. (**a**) Changes in conductivity of VO_2 with temperature under heating and cooling conditions; (**b**) absorber absorption spectra at different temperatures.

Similarly, we also studied the electric field diagrams of absorbers under different temperature conditions. As shown in Figures 7 and 8, we have plotted the electric field diagrams of the top and bottom VO_2 layers of the absorber when VO_2 is heated from 318 K to 345 K. We find that when the temperature rises, VO_2 changes from an insulating state to a metallic state, and the electric field intensity of the absorber increases. At the same time, local surface plasmon resonance occurs around the top disc-shaped VO_2 and the bottom circular hole VO_2 inner cavity, which enhances the absorption of light [54–56]. The electric field diagrams in Figures 7 and 8 also prove this.

In order to expand the application field of our absorber, we also conducted research on the structure of the circular hole in VO_2 thin film and VO_2 circular disk. We first studied the radius of the circular hole. With the change in the radius, the absorption curve of the absorber has changed, as shown in Figure 9a. When the circular hole radius is 0.23 μm, the maximum absorption rate of the two peaks from left to right is 30.24 THz and 44.03 THz, respectively, 99.95% and 99.64%. The minimum absorption rate between the two peaks is 88.24%. At this time, the absorption rate at 29.13–35.04 THz and 39.08–47.51 THz is higher than 90%, and the absorption bandwidth is 14.33 THz; When the radius of the circular hole gradually increases to 0.35 μm, the maximum absorptivity of the two peaks from left to right is 30.31 THz and 42.53 THz, 99.99% and 99.53%, respectively, and the minimum absorptivity between the two peaks is 93.04%. At this time, the absorptivity at 29.02–46.24 THz is higher than 90%, and the absorption bandwidth is 17.12 THz. In conclusion, when we adjust the radius of the circular hole from 0.23 μm to 0.35 μm, there is no significant impact on the absorptivity of the two absorption peaks of the absorber, But the absorption peak on the right has undergone a red shift, and the lowest absorption rate between the two peaks has increased [57,58]. Therefore, we can control the frequency of the absorption peak on the right and the lowest absorption rate of broadband absorption by adjusting the radius of the ring.

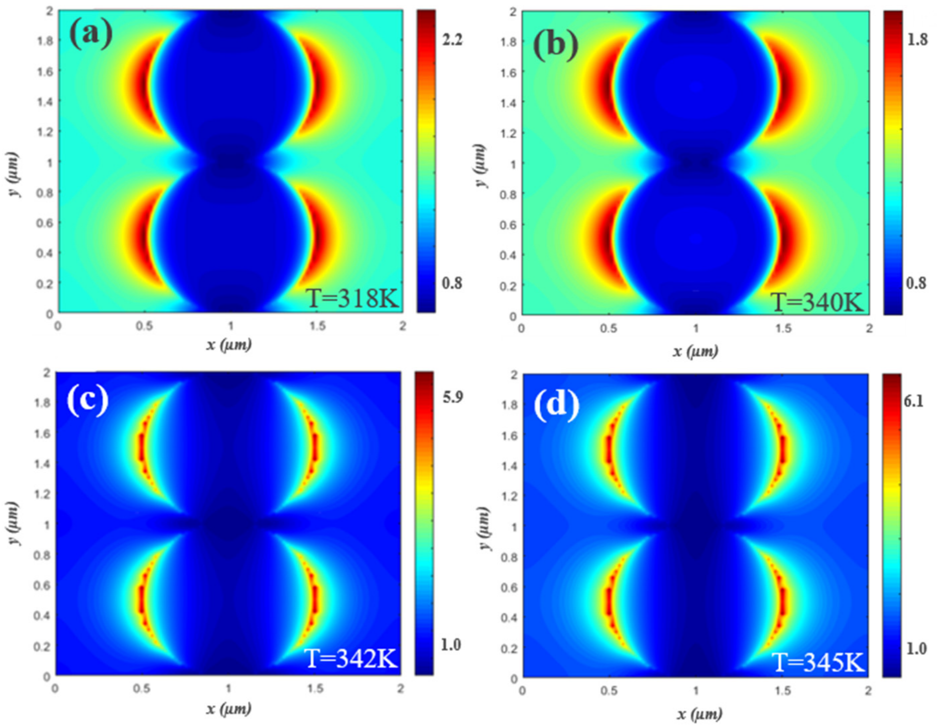

Figure 7. (**a**–**d**) Electric field diagrams of VO_2 in the upper layer of the absorber at different temperatures.

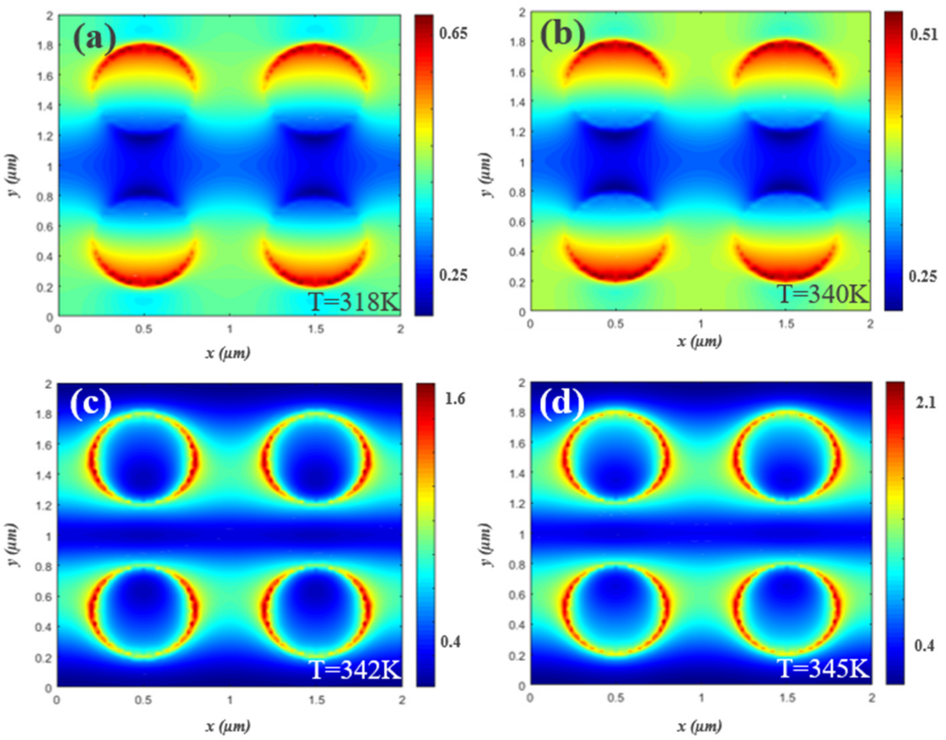

Figure 8. (**a**–**d**) Electric field diagrams of VO_2 in the lower layer of the absorber at different temperatures.

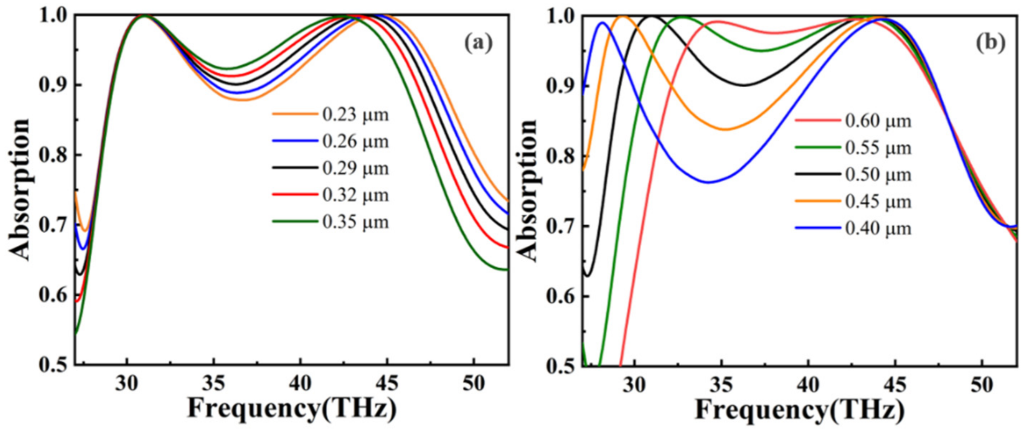

Figure 9. (**a**) Absorption spectra of VO_2 hole with radius of 0.23, 0.26, 0.29, 0.32, and 0.35 μm; (**b**) the absorption spectra of VO_2 disks with radius of 0.60, 0.55, 0.50, 0.45, and 0.40 μm.

Next, we will explore the effect of changing the radius of the disk on the absorber. Figure 9b shows the absorption spectrum when we adjusted the disk radius from 0.6 μm to 0.4 μm. We can intuitively see that as the radius decreases, the left peak of the absorber shifts from 26.12 THz blue to 34.63 THz, the absorption rate increased from 97.54% to 99.99% and then decreased to 98.12%, and the absorption rate of the right peak increases from 98.63% to 99.12%. However, the minimum absorption rate between the two peaks increases from 75.36% to 97.21%, and at a radius of 0.4 μm, the absorption rates at 34.11–44.36 THz are all greater than 97%; that is, the perfect absorption with an absorption bandwidth of 10.25 THz is achieved.

In order to study the practical value and advantages of our absorber, we also discussed the situation at different incidence angles [59,60]. The scanned images of TE and TM waves are shown in Figure 10 and are compared with other absorbers developed in recent years, as shown in Table 2 [61–65]. Figure 10a shows the scanning pattern of TE waves with changes in incident angle. We can see that the absorption curve of the TE wave with an absorption bandwidth of 30–47 THz at an incidence angle of 0–50° has always kept the absorptivity above 80%, and the absorptivity of the two absorption peaks has always been kept above 90%; since our absorber is asymmetric, the TM wave is slightly different from the TE wave, as shown in Figure 10b. When the incident angle is 0–50°, the absorption curve of TM wave is kept above 80% at the absorption bandwidth of 32–49 THz and above 90% at 41–45 THz. In summary, our absorber can still maintain a high absorption rate of over 80% when the incident angle is 0–50°, so it has good practical value [66,67].

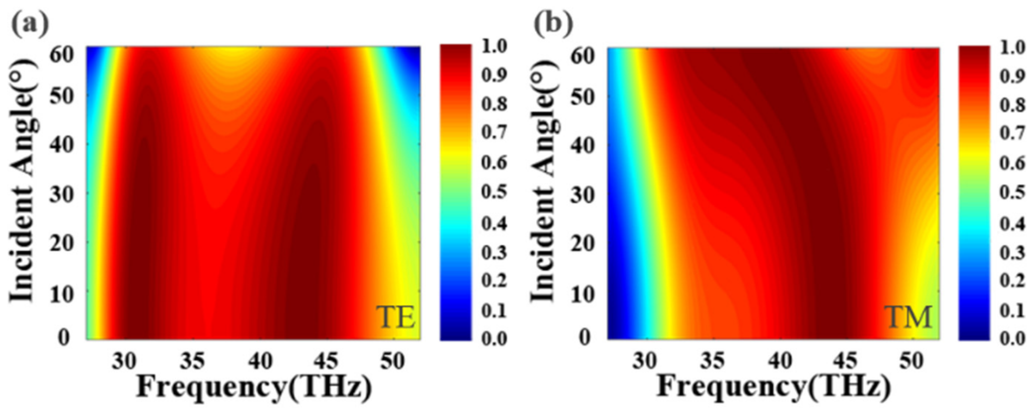

Figure 10. (**a**) TE wave scanning diagram; (**b**) TM wave scanning diagram.

Table 2. Comparison of absorbers in this article with other absorbers developed in recent years.

Reference	Operation Band	Max Absoptivity	Structure Layer
[61]	0.4–1.4 THz	96.3%	5
[62]	4.5–9.95 THz	99.9%	5
[63]	4.04–9.41 THz	99.5%	3
[64]	0.52–1.2 THz	98%	6
[65]	11–13 μm	99.9%	3
This work	29.1–47.2 THz	99.99%	5

5. Conclusions

This article proposes a temperature-tunable absorber based on VO_2, which consists of a VO_2 layer, dielectric layer, VO_2 layer, SiO_2 layer, and gold substrate from top to bottom. The top VO_2 layer is an array composed of double-disk patterns, and the bottom VO_2 layer is an array composed of four circular patterns, all of which are simple patterns and easy to process. We applied the PSO algorithm to determine the structure of our absorber and provided an optimization strategy suitable for our absorber, determining the optimal value within ten iterations. We drew the absorption spectrum of the absorber and found that the absorption bandwidth of 29.1–47.2 THz with an absorption rate higher than 90% was up to 18.1 THz, and there were two perfect absorption peaks in this range, with the absorption rates of 99.99% and 99.98%, respectively. Then, we explained the generation of absorption from the perspective of the electric field, and we studied the impact on the absorption curve of the absorber under the change in VO_2 temperature, which can be seen intuitively from the change in the electric field. Finally, we performed the change in absorption bandwidth and absorption rate of the absorber by adjusting the structure of VO_2 at the top and bottom. Through a comparison with other absorbers developed in recent years, we believe that our absorber has advantages in multiple aspects and is expected to deliver outstanding performance in fields such as photothermal absorption and thermal stealth in the future.

Author Contributions: Conceptualization, J.M., S.C. and Y.T.; data curation, J.M., J.C. (Jingyi Cheng), Z.Y. and B.T.; formal analysis, J.M. and J.C. (Jing Chen); methodology, Y.Y., P.W., J.C. (Jingyi Cheng), Z.Y. and T.S.; resources, Y.T., J.C. (Jing Chen) and Z.Y.; software, T.S., Y.T., S.C., J.C. (Jing Chen) and Y.Y.; data curation, Z.Y.; writing—original draft preparation, T.S.; writing—review and editing, J.M., Y.T., B.T., Y.Y., P.W. and T.S. All authors have read and agreed to the published version of the manuscript.

Funding: The authors are grateful to the support by National Natural Science Foundation of China (Nos. 11604311, 61705204, 21506257, 11974188); the funding provided by the Scientific Research Fund of Si Chuan Provincial Science and Technology Department (2020YJ0137; 2020YFG0467; 2021JDRC0019); the funding provided by the Open Fund of Hubei Key Laboratory of Mechanical Transmission and Manufacturing Engineering at Wuhan University of Science and Technology (MTMEOF2021B02); the funding provided by the Opening Project of Key Laboratory of Microelectronic Devices & Integrated Technology, Institute of Microelectronics, Chinese Academy of Sciences; the funding provided by the second batch of industry university cooperation collaborative education project in 2021 (202102153027); the funding provided by the Southwest University of Science and Technology College Students' Innovation and Entrepreneurship Training Program Project (S202210619103); the funding provided by the Southwest University of Science and Technology College Student Innovation Fund Project (CX22-063); and the funding provided by the 2022 Scientific Research Project of Huzhou College (2022HXKM07).

Institutional Review Board Statement: Not applicable.

Informed Consent Statement: Not applicable.

Data Availability Statement: Publicly available datasets were analyzed in this study. This data can be found here: https://www.lumerical.com/ (accessed on 1 January 2020).

Conflicts of Interest: The authors declare no conflict of interest.

References

1. Zhou, S.; Bi, K.; Li, Q.; Mei, L.; Niu, Y.; Fu, W.; Han, S.; Zhang, S.; Mu, J.; Tan, L.; et al. Patterned Graphene-Based Metamaterials for Terahertz Wave Absorption. *Coatings* **2023**, *13*, 59. [CrossRef]
2. Liang, S.R.; Xu, F.; Li, W.X.; Yang, W.X.; Cheng, S.B.; Yang, H.; Chen, J.; Yi, Z.; Jiang, P.P. Tunable smart mid infrared thermal control emitter based on phase change material VO_2 thin film. *Appl. Therm. Eng.* **2023**, *232*, 121074. [CrossRef]
3. Valagiannopoulos, C.; Sarsen, A.; Alù, A. Angular Memory of Photonic Metasurfaces. *IEEE Trans. Antennas Propag.* **2021**, *69*, 7720–7728. [CrossRef]
4. Liu, Y.N.; Li, X.H.; Yang, M.; Zhao, J.J.; Wang, W.J. Study on Dynamic Characteristics of the Bistable Nonlinear Damper. *Appl. Sci.* **2023**, *13*, 878. [CrossRef]
5. Valagiannopoulos, C.A. Effect of cylindrical scatterer with arbitrary curvature on the features of a metamaterial slab antenna. *Prog. Electromagn. Res. PIER* **2007**, *71*, 59–83. [CrossRef]
6. Han, J.; Li, L.; Tian, S.; Ma, X.; Feng, Q.; Liu, H.; Zhao, Y.; Liao, G. Frequency-Diverse Holographic Metasurface Antenna for Near-Field Microwave Computational Imaging. *Front. Mater.* **2021**, *8*, 766889. [CrossRef]
7. Landy, N.I.; Sajuyigbe, S.; Mock, J.J.; Smith, D.R.; Padilla, W.J. Perfect metamaterial absorber. *Phys. Rev. Lett.* **2008**, *100*, 207402. [CrossRef]
8. Zhang, Y.X.; Pu, M.B.; Jin, J.J.; Lu, X.J.; Guo, Y.H.; Cai, J.; Zhang, F.; Ha, Y.; He, Q.; Xu, M.; et al. Crosstalk-free achromatic full Stokes imaging polarimetry metasurface enabled by polarization-dependent phase optimization. *Opto-Electron. Adv.* **2022**, *5*, 220058. [CrossRef]
9. Wu, X.; Li, Y.; Xiang, Y.; Liu, Z.; He, Z.; Wu, X.; Li, Y.; Xiong, L.; Li, C.; Chen, J. Mixed-valence cobalt oxides bifunctional electrocatalyst with rich oxygen vacancies for aqueous metal-air batteries. *Chem. Eng. J.* **2023**, *453*, 139831. [CrossRef]
10. Qin, F.; Chen, J.; Liu, J.W.; Liu, L.; Tang, C.J.; Tang, B.; Li, G.F.; Zeng, L.C.; Li, H.L.; Yi, Z. Design of high efficiency perovskite solar cells based on inorganic and organic undoped double hole layer. *Sol. Energy* **2023**, *262*, 111796. [CrossRef]
11. Krasikov, S.; Tranter, A.; Bogdanov, A.; Kivshar, Y. Intelligent metaphotonics empowered by machine learning. *Opto-Electron. Adv.* **2022**, *5*, 210147. [CrossRef]
12. Chen, Z.H.; Cai, P.G.; Wen, Q.Y.; Chen, H.; Tang, Y.J.; Yi, Z.; Wei, K.H.; Li, G.F.; Tang, B.; Yi, Y.G. Graphene Multi-Frequency Broadband and Ultra-Broadband Terahertz Absorber Based on Surface Plasmon Resonance. *Electronics* **2023**, *12*, 2655. [CrossRef]
13. Gao, S.Y.; Wei, K.H.; Yang, H.; Tang, Y.J.; Yi, Z.; Tang, C.J.; Tang, B.; Yi, Y.G.; Wu, P.H. Design of Surface Plasmon Resonance-Based D-Type Double Open-Loop Channels PCF for Temperature Sensing. *Sensors* **2023**, *23*, 7569. [CrossRef]
14. Li, C.; Shi, X.; Liang, S.; Ma, X.; Han, M.; Wu, X.; Zhou, J. Spatially homogeneous copper foam as surface dendrite-free host for zinc metal anode. *Chem. Eng. J.* **2020**, *379*, 122248. [CrossRef]
15. Zheng, Z.; Xu, L.; Huang, L.J.; Smirnova, D.; Kamali, K.Z.; Yousefi, A.; Deng, F.; Camacho-Morales, R.; Ying, C.; Miroshnichenko, A.E.; et al. Third-harmonic generation and imaging with resonant Si membrane metasurface. *Opto-Electron. Adv.* **2023**, *6*, 220174. [CrossRef]
16. Zhou, Z.; Liu, W.; Guo, Y.; Huang, H.; Ding, X. Design Simulation and Optimization of Germanium-Based Solar Cells with Micro-Nano Cross-Cone Absorption Structure. *Coatings* **2022**, *12*, 1653. [CrossRef]
17. Lai, R.; Shi, P.; Yi, Z.; Li, H.; Yi, Y. Triple-Band Surface Plasmon Resonance Metamaterial Absorber Based on Open-Ended Prohibited Sign Type Monolayer Graphene. *Micromachines* **2023**, *14*, 953. [CrossRef] [PubMed]
18. Wu, X.W.; Li, Y.H.; Li, C.C.; He, Z.X.; Xiang, Y.H.; Xiong, L.Z.; Chen, D.; Yu, Y.; Sun, K.; He, Z.Q.; et al. The electrochemical performance improvement of $LiMn_2O_4/Zn$ based on zinc foil as the current collector and thiourea as an electrolyte additive. *J. Power Sources* **2015**, *300*, 453–459. [CrossRef]
19. Ma, X.; Song, R.; Fan, Z.; Zhou, S. Phase-Change Metasurface by U-Shaped Atoms for Photonic Switch with High Contrast Ratio. *Coatings* **2021**, *11*, 1499. [CrossRef]
20. Sorathiya, V.; Lavadiya, S.; Thomas, L.; Abd-Elnaby, M.; Rashed, A.N.Z.; Eid, M.M.A. Graphene-based tunable short band absorber for infrared wavelength. *Appl. Phys. B* **2022**, *128*, 40. [CrossRef]
21. Zhu, Y.Y.; Cai, P.G.; Zhang, W.L.; Meng, T.Y.; Tang, Y.J.; Yi, Z.; Wei, K.H.; Li, G.F.; Tang, B.; Yi, Y.G. Ultra-Wideband High-Efficiency Solar Absorber and Thermal Emitter Based on Semiconductor InAs Microstructures. *Micromachines* **2023**, *14*, 1597. [CrossRef] [PubMed]
22. Liu, W.; Liu, C.; Wang, J.X.; Lv, J.W.; Lv, Y.; Yang, L.; An, N.; Yi, Z.; Liu, Q.; Hu, C.J.; et al. Surface plasmon resonance sensor composed of microstructured optical fibers for monitoring of external and internal environments in biological and environmental sensing. *Results Phys.* **2023**, *47*, 106365. [CrossRef]
23. Morin, F.J. Oxides Which Show a Metal-to-Insulator Transition at the Neel Temperature. *Phys. Rev. Lett.* **1959**, *3*, 34–36. [CrossRef]
24. Zhong, M. A multi-band metamaterial absorber based on VO_2 layer. *Opt. Laser Technol.* **2021**, *139*, 106930. [CrossRef]
25. Ri, K.J.; Kim, J.S.; Kim, J.H.; Ri, C.H. Tunable triple-broadband terahertz metamaterial absorber using a single VO_2 circular ring. *Opt. Commun.* **2023**, *542*, 129573. [CrossRef]
26. Otair, M.; Ibrahim, O.T.; Abualigah, L.; Altalhi, M.; Sumari, P. An enhanced Grey Wolf Optimizer based Particle Swarm Optimizer for intrusion detection system in wireless sensor networks. *Wirel. Netw.* **2022**, *28*, 721–744. [CrossRef]
27. Zhou, W.; Qin, X.; Lv, M.; Qiu, L.; Chen, Z.; Zhang, F. Design of a New Type of In-Hole Gold-Coated High-Performance Quasi-PCF Sensor Enhanced with Surface Plasmon Resonance. *Coatings* **2023**, *13*, 1261. [CrossRef]

28. Guo, Y.M.; Zhong, L.B.; Min, L.; Wang, J.Y.; Wu, Y.; Chen, K.L.; Wei, K.; Rao, C.H. Adaptive optics based on machine learning: A review. *Opto-Electron. Adv.* **2022**, *5*, 200082. [CrossRef]
29. Cui, S.F.; Liu, J.F.; Chen, X.L.; Li, Q. Experimental Analysis of Gas Holdup Measured by Gas Array Tool in Gas–Water Two Phase of Horizontal Well. *Coatings* **2021**, *11*, 343. [CrossRef]
30. Xu, L.; Zeng, J.; Luo, X.; Xia, L.; Ma, Z.; Peng, B.; Li, Z.; Zhai, X.; Wang, L. Dual-Band Plasmonic Perfect Absorber Based on the Hybrid Halide Perovskite in the Communication Regime. *Coatings* **2021**, *11*, 67. [CrossRef]
31. Alterazi, H.A.; Kshirsagar, P.R.; Manoharan, H.; Selvarajan, S.; Alhebaishi, N.; Srivastava, G.; Lin, J.C.-W. Prevention of Cyber Security with the Internet of Things Using Particle Swarm Optimization. *Sensors* **2022**, *22*, 6117. [CrossRef]
32. Qi, B.X.; Shou, H.J.; Zhang, J.W.; Chen, W.Q.; Feng, J.L.; Niu, T.M.; Mei, Z.L. A near-perfect metamaterial selective absorber for high-efficiency solar photothermal conversion. *Int. J. Therm. Sci.* **2023**, *194*, 108580. [CrossRef]
33. Pan, M.; Huang, H.; Chen, W.; Li, S.; Xie, Q.; Xu, F.; Wei, D.; Fang, J.; Fan, B.; Cai, L. Design of Narrow-Band Absorber Based on Symmetric Silicon Grating and Research on Its Sensing Performance. *Coatings* **2021**, *11*, 553. [CrossRef]
34. Tang, F.; Wu, X.; Shen, Y.; Xiang, Y.; Wu, X.; Xiong, L.; Wu, X. The intercalation cathode materials of heterostructure MnS/MnO with dual ions defect embedded in N-doped carbon fibers for aqueous zinc ion batteries. *Energy Storage Mater.* **2022**, *52*, 180–188. [CrossRef]
35. Fan, H.Y.; Li, J.; Lai, Y.; Luo, J. Optical Brewster metasurfaces exhibiting ultrabroadband reflectionless absorption and extreme angular asymmetry. *Phys. Rev. Appl.* **2021**, *16*, 044064. [CrossRef]
36. Wu, X.; Tan, C.; He, C.; Zhao, T.; Wu, X.; Ma, Z.; Wang, H.; Cai, Y.; Wu, Q.; Li, Q. Strategy for boosting Co-Nx content for oxygen reduction reaction in aqueous metal-air batteries. *J. Power Sources* **2022**, *520*, 230891. [CrossRef]
37. Zheng, Y.; Yi, Z.; Liu, L.; Wu, X.W.; Liu, H.; Li, G.F.; Zeng, L.C.; Li, H.L.; Wu, P.H. Numerical simulation of efficient solar absorbers and thermal emitters based on multilayer nanodisk arrays. *Appl. Therm. Eng.* **2023**, *230*, 120841. [CrossRef]
38. Lu, C.; Lu, Q.; Gao, M.; Lin, Y. Dynamic Manipulation of THz Waves Enabled by Phase-Transition VO_2 Thin Film. *Nanomaterials* **2021**, *11*, 114. [CrossRef]
39. Shin, J.-H.; Park, K.H.; Ryu, H.-C. A Band-Switchable and Tunable THz Metamaterial Based on an Etched Vanadium Dioxide Thin Film. *Photonics* **2022**, *9*, 89. [CrossRef]
40. Chen, M.M.; Yang, X.X. Tunable and three-dimensional dual-band metamaterial absorber based on electromagnetically induced transparency with vanadium dioxide. *Phys. Chem. Chem. Phys.* **2023**, *25*, 13393–13398. [CrossRef]
41. Kim, M.K.; Lee, D.S.; Yang, Y.H.; Rho, J.S. Switchable diurnal radiative cooling by doped VO_2. *Opto-Electron. Adv.* **2021**, *4*, 200006. [CrossRef]
42. Qi, Y.P.; Wang, L.; Wen, Y.J.; Chen, H.W.; Yuan, Y.J.; Zhou, Z.H.; Zhao, S.Y.; Wang, X.X. Design of a switchable bifunctional terahertz metamaterial absorber from ultra-broadband to 10-band. *J. Opt. Soc. Am. B* **2023**, *40*, 939–948. [CrossRef]
43. Zhu, R.; Wang, J.; Sui, S.; Meng, Y.; Qiu, T.; Jia, Y.; Wang, X.; Han, Y.; Feng, M.; Zheng, L.; et al. Wideband Absorbing Plasmonic Structures via Profile Optimization Based on Genetic Algorithm. *Front. Phys.* **2020**, *8*, 231. [CrossRef]
44. Wu, F.Y.; Shi, P.C.; Yi, Z.; Li, H.L.; Yi, Y.G. Ultra-Broadband Solar Absorber and High-Efficiency Thermal Emitter from UV to Mid-Infrared Spectrum. *Micromachines* **2023**, *14*, 985. [CrossRef]
45. Li, Y.; Yang, S.; Du, H.; Liu, Y.; Wu, X.; Yin, C.; Wang, D.; Wu, X.; He, Z.; Wu, X. A stable fluoride-based interphase for a long cycle Zn metal anode in an aqueous zinc ion battery. *J. Mater. Chem. A* **2022**, *10*, 14399–14410. [CrossRef]
46. Wang, B.X.; Wu, C.Y.; Duan, G.Y.; Xu, W.; Pi, F.W. Review of broadband metamaterial absorbers: From principles, design strategies, and tunable properties to functiona applications. *Adv. Funct. Mater.* **2023**, *33*, 2213818. [CrossRef]
47. Li, J.; Liu, G.; Liu, B.; Min, Z.; Qian, D.; Jiang, J.; Li, J. An extremely facile route to Co_2P encased in N,P-codoped carbon layers: Highly efficient bifunctional electrocatalysts for ORR and OER. *Int. J. Hydrogen Energy* **2018**, *3*, 1365–1374. [CrossRef]
48. Chen, H.; Li, W.; Zhu, S.M.; Hou, A.Q.; Liu, T.; Xu, J.S.; Zhang, X.W.; Yi, Z.; Yi, Y.G.; Dai, B. Study on the Thermal Distribution Characteristics of a Molten Quartz Ceramic Surface under Quartz Lamp Radiation. *Micromachines* **2023**, *14*, 1231. [CrossRef]
49. Zhu, L.; Hu, R.; Xiang, Y.; Yang, X.; Chen, Z.; Xiong, L.; Wu, X.; He, Z.; Lei, W. Enhanced performance of Li-S battery by constructing inner conductive network and outer adsorption layer sulfur-carbon composite. *Int. J. Energy Res.* **2020**, *45*, 6002–6014. [CrossRef]
50. Shan, L.; Zhou, J.; Zhang, W.; Xia, C.; Guo, S.; Ma, X.; Fang, G.; Wu, X.; Liang, S. Highly Reversible Phase Transition Endows V_6O_{13} with Enhanced Performance as Aqueous Zinc-Ion Battery Cathode. *Energy Technol.* **2019**, *7*, 57. [CrossRef]
51. Sharbirin, A.S.; Akhtar, S.; Kim, J.Y. Light-emitting MXene quantum dots. *Opto-Electron. Adv.* **2021**, *4*, 200077. [CrossRef]
52. Garry, G.; Durand, O.; Lordereau, A. Structural, electrical and optical properties of pulsed laser deposited VO_2 thin films on R- and C-sapphire planes. *Thin Solid Film.* **2004**, *453–454*, 427–430. [CrossRef]
53. Case, F.C. Modifications in the phase transition properties of predeposited VO_2 films. *J. Vac. Sci. Technol. A Vac. Surf. Film.* **1984**, *2*, 1509–1512. [CrossRef]
54. Maksimovic, J.; Hu, J.W.; Ng, S.H.; Katkus, T.; Seniutinas, G.; Rivera, T.P.; Stuiber, M.; Nishijima, Y.; John, S.; Juodkazis, S. Beyond Lambertian light trapping for large-area silicon solar cells: Fabrication methods. *Opto-Electron. Adv.* **2022**, *5*, 210086. [CrossRef]
55. Meng, W.; Li, C.; Yao, M.; He, Z.; Wu, X.; Jiang, Z.; Dai, L.; Wang, L. Synthesis and electrochemical performance of $Li_{1+x}Ti_{2-x}Fe_x(PO_4)_3$/C anode for aqueous lithium ion battery. *Adv. Powder Technol.* **2020**, *31*, 1359–1364. [CrossRef]
56. Wu, X.; Li, Y.; Xiang, Y.; Liu, Z.; He, Z.; Wu, X.; Li, Y.; Xiong, L.; Li, C.; Chen, J. The electrochemical performance of aqueous rechargeable battery of $Zn/Na_{0.44}MnO_2$ based on hybrid electrolyte. *J. Power Sources* **2016**, *336*, 35–39. [CrossRef]

57. Liu, Y.; Wang, Z.; Li, L.; Gao, S.; Zheng, D.; Yu, X.; Wu, Q.; Yang, Q.; Zhu, D.; Yang, W.; et al. Highly efficient quantum-dot-sensitized solar cells with composite semiconductor of ZnO nanorod and oxide inverse opal in photoanode. *Electrochim. Acta* **2022**, *412*, 140145. [CrossRef]
58. Chen, M.M.; Yang, X.X. High-transmission and large group delay terahertz triple-band electromagnetically induced transparency in a metal-perovskite hybrid metasurface. *Phys. Chem. Chem. Phys.* **2023**, *25*, 21547–21553. [CrossRef]
59. Sui, J.Y.; Liao, S.Y.; Dong, R.Y.; Zhang, H.F. A Janus Logic Gate with Sensing Function. *Ann. Phys.* **2023**, *535*, 2200661. [CrossRef]
60. Revollo, H.; Ferrada, P.; Martin, P.; Marzo, A.; del Campo, V. HIT Solar Cell Modeling Using Graphene as a Transparent Conductive Layer Considering the Atacama Desert Solar Spectrum. *Appl. Sci.* **2023**, *13*, 9323. [CrossRef]
61. Liu, W.; Song, Z. Terahertz absorption modulator with largely tunable bandwidth and intensity. *Carbon.* **2021**, *174*, 617–624. [CrossRef]
62. Luo, X.; Tan, R.; Li, Q.; Chen, J.; Xie, Y.; Peng, J.; Zeng, M.; Jiang, M.; Wu, C.; He, Y. High-sensitivity long-range surface plasmon resonance sensing assisted by gold nanoring cavity arrays and nanocavity coupling. *Phys. Chem. Chem. Phys.* **2023**, *25*, 9273–9281. [CrossRef]
63. Zhang, L.; Liu, W.; Cencillo-Abad, P.; Wang, Q.; Huang, X.; Leng, Y. A tunable broadband polarization-independent metamaterial terahertz absorber based on VO_2 and Dirac semimetal. *Opt. Commun.* **2023**, *542*, 129602. [CrossRef]
64. Song, Z.; Zhang, J. Achieving broadband absorption and polarization conversion with a vanadium dioxide metasurface in the same terahertz frequencies. *Opt. Express* **2020**, *28*, 12487–12497. [CrossRef] [PubMed]
65. Wang, H.; Yang, Y.; Wang, L. Wavelength-tunable infrared metamaterial by tailoring magnetic resonance condition with VO_2 phase transition. *J. Appl. Phys.* **2014**, *116*, 123503. [CrossRef]
66. He, K.; Ning, T.G.; Li, J.; Pei, L.; Bai, B.; Wang, J.S. Light manipulation for all-fiber devices with VCSEL and graphene-based metasurface. *Opt. Express* **2023**, *31*, 29627–29638. [CrossRef]
67. Zhou, Z.Y.; Liu, W.F.; Huang, H.L.; Ding, X.L.; Li, X.T. Enhancement of Photoelectric Performance Based on Ultrathin Wide Spectrum Solar Absorption in Cruciform Microstructure Germanium Solar Cells. *Coatings* **2023**, *13*, 1123. [CrossRef]